

How the Coherent Tides Obstruct the Radial Infalls of Satellite Galaxies onto Clusters

Jounghun Lee

*Astronomy Program, Department of Physics and Astronomy, Seoul National University,
Seoul 08826, Republic of Korea*

jounghun@astro.snu.ac.kr

ABSTRACT

A direct numerical evidence for the obstructing effect of the coherent tides on the infall-zone satellites around the cluster halos is presented. Analyzing the numerical data from a high-resolution N-body simulation, we calculate the mean fractions of the radial and tangential velocities of the infall-zone satellites around the cluster halos and investigate if and how they depend on the tidal coherence defined as the alignments between the major principal axes of the local tidal fields smoothed on the linear and nonlinear scales. It is found that the infall-zone satellites located in the regions with higher tidal coherence have significantly smaller and larger mean fractions of the radial and tangential velocities, respectively, which indicates that the radial infall of satellites onto host clusters are obstructed by the coherent tides. We also show that those satellites separated by shorter distances from the host clusters, having lower-masses, and embedded in the anisotropic large-scale environments like filaments and sheets, are more vulnerable to the obstructing effect of the coherent tides.

Subject headings: cosmology:theory — large-scale structure of universe

1. Introduction

A recent numerical study of Borzyszkowski et al. (2017) based on a zoomed N-body simulation has revealed that the thickness of a filament affects the growth history of its constituent halos. According to its result, the galactic halos located in the conjunction of multiple fine filaments grow through "accretion" of matter onto them along the filaments, while the growths of those embedded in a broad bulky filament are quenched by the recession of matter from them in the plane perpendicular to the filament axis (see also Garaldi et al.

2017). Given this result, Borzyszkowski et al. (2017) claimed that the difference in the clustering pattern between the galactic halos embedded in the former and latter environments should be the origin of the halo assembly bias (Gao & White 2007), which had been a long standing puzzle in the standard theory of structure formation.

Lee (2018a) suggested that it should be desirable to use a more quantitative unequivocal criterion for the classification of the tidal environments rather than using such a qualitative equivocal description as a bulky broad filament or multiple fine filaments for a systematic study of the large-scale tidal effect on the growth history of the halos. Assuming that a broad bulky filament forms through two dimensional collapse of an over dense region along the coherent direction of the principal axes of the underlying tidal field over large scales, they introduced a new concept, "tidal coherence", quantitatively defining it as the alignments between the major principal axes of the local tidal fields smoothed on the nonlinear and linear scales. Utilizing the data from the Sloan Digital Sky Survey Data Release 10 (Ahn et al. 2014), Lee (2018a) detected a strong tendency for the less (more) luminous galaxies to populate the regions with higher (lower) tidal coherence even when the dominant effect of the local densities was nullified. Lee (2018a) espoused the same logic of Borzyszkowski et al. (2017) to explain this observed tendency: The coherent tides quench the growth of the galaxies by obstructing the radial flow of satellites and matter onto the galaxies.

In this Letter, we attempt to find a direct numerical evidence for the obstructing effect of the coherent tides on the satellites by examining the directions of the satellite motions relative to their hosts and their links to the degree of the tidal coherence in the regions where the hosts reside. If the observed anti-correlation between the galaxy luminosity and the degree of the tidal coherence is truly caused by the obstructing effect of the coherent tides on the motions of satellites and matter as speculated by Lee (2018a), then those satellites located in the regions with higher tidal coherence must have relatively larger (smaller) fractions of the tangential (radial) velocities. To avoid poor number statistics and contaminations caused by low particle resolution, we will use as our host objects the cluster halos which have much larger number of satellites than the galactic halos. Throughout this Letter, we will assume a Planck Λ CDM (Λ + cold dark matter) universe (Planck Collaboration et al. 2014).

2. Numerical Analysis

To investigate how the coherent tides affect the motions of the neighbor halos around the cluster halos, we analyze the numerical data extracted from the high-resolution Small MultiDark PLanck simulation (SMDPL) (Klypin et al. 2016), a pure DM N -body simulation performed as one of the MultiDark simulation series (Riebe et al. 2013). The box size

(L_{box}), total number of DM particles (N_p), and mass of an individual DM particle (m_p) of the SMDPL are as follows: $L_{\text{box}} = 400 h^{-1}\text{Mpc}$, $N_p = 3840^3$ and $m_p = 9.63 \times 10^7 h^{-1} M_\odot$ (doi:10.17876/cosmosim/smdpl/). Klypin et al. (2016) applied the Rockstar halo finder (Behroozi et al. 2013) to the particle distributions from the SMPDL to compile a catalog of the DM halos and subhalos at various redshifts from $z = 120$ to $z = 0$. They also employed the cloud-in-cell method to construct the density field, $\delta(\mathbf{x})$, of DM particles on a total of 512^3 cubic grids which constitute the simulation volume at $z = 0$.

To measure the tidal coherence, q , at each of the 512^3 grids, we use the tidal fields constructed from the density fields in our previous work (Lee 2018b) with the help of the Fast Fourier Transformation (FFT) code (Press et al. 1992). Let us briefly describe how the construction of $\mathbf{T}(\mathbf{x})$ proceeds: The first step is to smooth the density field with a Gaussian filter on a linear scale of $R_f = 30 h^{-1}\text{Mpc}$ and then to find the Fourier amplitude, $\tilde{\delta}(\mathbf{k})$, of the smoothed density field, $\delta(\mathbf{x})$, via the FFT code. Here, the choice of the linear scale is made given the finding of Pandey & Sarkar (2017) that the influence of the large-scale environments on the galaxy properties persists at non-negligible level up to the scale of $30 h^{-1}\text{Mpc}$.

The second step is to compute the nine components of the Fourier amplitude of the tidal field as $\tilde{T}_{ij} = k_i k_j \tilde{\delta}(\mathbf{k})/k^2$ where $i, j \in \{1, 2, 3\}$ and $\mathbf{k} = (k_i)$ is a wave vector dual to \mathbf{x} in the Fourier space. The third step is to obtain the tidal field, $\mathbf{T}(\mathbf{x})$, from $\tilde{\mathbf{T}}(\mathbf{k})$ through the inverse FFT code and then to find a set of three eigenvalues, $\{\lambda_1, \lambda_2, \lambda_3 | \lambda_1 \geq \lambda_2 \geq \lambda_3\}$ and corresponding eigenvectors, $\{\mathbf{e}_1, \mathbf{e}_2, \mathbf{e}_3\}$, via the similarity transformation of $\mathbf{T}(\mathbf{x})$ at each grid. The whole process is repeated but on a nonlinear scale of $R'_f = 2 h^{-1}\text{Mpc}$ (a typical cluster size) to obtain a new set of three eigenvalues and eigenvectors, $\{\lambda'_1, \lambda'_2, \lambda'_3 | \lambda'_1 \geq \lambda'_2 \geq \lambda'_3\}$ and $\{\mathbf{e}'_1, \mathbf{e}'_2, \mathbf{e}'_3\}$ at each grid.

Following the original definition of Lee (2018a), we determine the tidal coherence, q , at each grid as $q = |\mathbf{e}_1 \cdot \mathbf{e}'_1|$ whose value lies in the range of $[0, 1]$. A larger value of q translates into a highly coherent tide. Here, a highly coherent tide represents the gravitational collapse of matter along the major principal axis of the local tidal field whose direction is coherent over a wide range of the scale (from $2 h^{-1}\text{Mpc}$ to $30 h^{-1}\text{Mpc}$). From the Rockstar halo catalog at $z = 0$ extracted from the CosmoSim database (doi:10.17876/cosmosim/smdpl/), we first select a total of 1659 cluster-size halos with virial masses of $M_h \geq 10^{14} h^{-1} M_\odot$. Tagging each of the selected cluster halos with the value of q at the grid point where it is placed, we separate the cluster halos into four q -selected samples (see Table 1). Hereafter, we are going to use interchangeably the terms, host cluster halos, host clusters, and hosts.

For each host, we search for its neighbor halos with virial masses of $M_s \geq 10^{11} h^{-1} M_\odot$ in the distance range of $1 \leq r/r_v < 3$ with $r \equiv |\mathbf{r}|$, where r_v is the virial radius of a host

and \mathbf{r} is the separation vector from the host center. The DM halos with virial masses lower than $10^{11} h^{-1} M_{\odot}$ composed of less than 1000 DM particles are excluded from the current analysis to avoid any numerical contamination caused by the low resolution. The distance range of $1 \leq r/r_v < 3$ is called the infall zone where the gravitational influence of a host overwhelms the Hubble flow (Zu et al. 2014). Expecting that the neighbor halos located in the infall zone of a host will become its satellites, we are going to refer to them as *infall-zone satellites* throughout this work.

The fraction of the radial and tangential components of \mathbf{v} are defined as $\delta v_r = |\mathbf{v} \cdot \hat{\mathbf{r}}|/v$ and $\delta v_t = |\mathbf{v} - \mathbf{v}_r \hat{\mathbf{r}}|/v$, respectively, where $\hat{\mathbf{r}} \equiv \mathbf{r}/r$ and $v \equiv |\mathbf{v}|$ (see Figure 1). Finally, two ensemble averages, $\langle \delta v_r \rangle$ and $\langle \delta v_t \rangle$, are taken over the infall-zone satellites of the host clusters belonging to each q -selected sample. The errors in the measurement of the two averages, σ_t and σ_r , are also estimated as the standard deviations in the mean values as $\sigma_t = \sqrt{[(\langle \delta v_t \rangle^2) - \langle \delta v_t^2 \rangle] / (N_h - 1)}$ and $\sigma_r = \sqrt{[(\langle \delta v_r \rangle^2) - \langle \delta v_r^2 \rangle] / (N_h - 1)}$ where N_h is the number of the host halos belonging to each sample.

Figure 2 shows the values of $\langle \delta v_t \rangle$ and $\langle \delta v_r \rangle$ with errors from the four q -selected samples in the top and bottom panels, respectively. It can be clearly seen that the samples with higher- q values yield higher and lower mean fractions of the tangential and radial velocities, respectively, indicating a detection of significant signals of $\langle \delta v_t \rangle$ - q correlation and $\langle \delta v_r \rangle$ - q anti-correlation. Although all of the four q -selected samples yield $\langle \delta v_r \rangle > \langle \delta v_t \rangle$, the difference between the two averages becomes smaller as q increases. In fact, in the highest- q range of $0.9 < q \leq 1$ the value of $\langle \delta v_r \rangle$ becomes quite comparable to that of $\langle \delta v_t \rangle$.

Yet, before interpreting the $\langle \delta v_t \rangle$ - q correlation and $\langle \delta v_r \rangle$ - q anti-correlation shown in Figure 2 as a direct evidence for the existence of the obstructing effect of the coherent tides on the radial motions of the infall-zone satellites, an additional verification process is required: Since the same trend could be produced even when the coherent tides only facilitate the tangential motions of the infall-zone satellites without significantly obstructing their radial motions, it has to be investigated if and how the mean values of the tangential and radial velocities themselves vary with q . For this investigation, it is first necessary to deal with the differences among the four q -selected samples in the distributions of the host halo masses and separation distances of the infall-zone satellites, since the mean value of the total velocity, $\langle v \rangle$, depends most sensitively on M_h and r . The top panel of Figure 3 shows how the mass distributions of the host clusters from the four q -selected samples differ from one another. Taking the same number of the host clusters at each bin of M_h , we control the four q -selected samples to have the identical mass distributions, which are shown in the bottom panel of Figure 3. In a similar manner, we also control further the four samples to have identical distributions of the separation distances of the infall-zone satellites around

the host clusters. Figure 4 plots the original and controlled number distributions of the infall-zone satellites versus r in the top and bottom panels, respectively.

We compute the values of $\langle v_t \rangle$ and $\langle v_r \rangle$ from the four controlled samples and plot them versus q in Figure 5, which clearly reveals the existence of both of the $\langle v_t \rangle$ - q correlation and $\langle v_r \rangle$ - q anti-correlation. Note, however, that the $\langle v_r \rangle$ - q anti-correlation is more significant in strength than the $\langle v_t \rangle$ - q correlation: the value of $\langle v_r \rangle$ shows almost monotonic decrease with q in the entire range of q , while that of $\langle v_t \rangle$ does not significantly increase with q in the range of $0 < q \leq 0.7$, showing a rapid rise only in the highest q range of $0.9 < q \leq 1$. This result indicates that although the coherent tides simultaneously obstruct and facilitate the radial and tangential motions of the infall-zone satellites, respectively, the former effect is more dominant. It confirms the speculation of Lee (2018a) that the growths of the host clusters located in the regions with higher tidal coherence would be delayed compared with those in the regions with lower tidal coherence because the radial infalls of their satellites are obstructed by the coherent tides.

To see whether or not the degree of the vulnerability to the obstructing effect of the coherent tides depends on the masses of the infall-zone satellites, we take the averages, $\langle \delta v_t \rangle$ and $\langle \delta v_r \rangle$, over the infall-zone satellites in the low-mass ($1 \leq M_s/[10^{11} h^{-1} M_\odot] < 5$) and high-mass ($M_s/[10^{11} h^{-1} M_\odot] \geq 5$) ranges separately, the results of which are shown in the left and right panels of Figure 6. The results shown in Figure 2 (i.e., the results obtained without constraining the range of M_s) are also shown as dotted lines for comparison in Figure 6. Both of the low-mass and high-mass cases exhibit the same trend as that shown in Figure 2: the $\langle \delta v_t \rangle$ - q correlation and the $\langle \delta v_r \rangle$ - q anti-correlation. As can be witnessed, however, the low-mass infall-zone satellites yield much larger values of $\langle \delta v_t \rangle$ than the high-mass counterparts in the whole range of q .

Note that the value of $\langle \delta v_t \rangle$ exceeds that of $\langle \delta v_r \rangle$ in the range of $0.9 \leq q < 1$ for the low-mass case while the increment of $\langle \delta v_t \rangle$ with q or equivalently the decrement of $\langle \delta v_r \rangle$ with q are more rapid for the high-mass case. Our explanation for this result is as follows. The strong gravitational attraction between the high-mass satellites and their host clusters can resist the obstructing effect of the weakly coherent tides (i.e., low value of q), while the low-mass satellites are so vulnerable to the tidal effects that their radial infall toward their hosts are readily obstructed even by the weakly coherent tides.

Taking the averages over the satellites in the inner ($1 \leq r/r_v < 2$) and outer ($2 \leq r/r_v < 3$) infall zones separately, we investigate how the strengths of $\langle \delta v_t \rangle$ - q correlation and $\langle \delta v_r \rangle$ - q anti-correlation depend on the separation distance, r , the results of which are shown in Figure 7. As can be seen, the inner infall-zone satellites yield much larger values of $\langle \delta v_t \rangle$ than the outer infall-zone counterparts in the entire range of q . For the case of the inner

infall-zone satellites, the value of $\langle \delta v_t \rangle$ is comparable to that $\langle \delta v_r \rangle$ even in the lowest q -range of $0 \leq q < 0.4$. Furthermore, $\langle \delta v_t \rangle$ exceeds $\langle \delta v_r \rangle$ in the higher- q range of $0.4 \leq q < 1$. Whereas, the outer infall-zone satellites are found to have $\langle \delta v_t \rangle < \langle \delta v_r \rangle$ in the entire range of q , although they still exhibit the $\langle \delta v_t \rangle$ - q correlation and $\langle \delta v_r \rangle$ - q anti-correlation. This phenomenon can be understood given that the inner infall-zone satellites must have been exposed to the obstructing effect of the coherent tides for longer period of time than the outer infall-zone counterparts since they entered the infall zones of their hosts at earlier epochs.

Another interesting issue is if and how the type of the cosmic web affects the behaviors of $\langle \delta v_r \rangle$ and $\langle \delta v_t \rangle$. To address this issue, we apply the conventional web-classification algorithm suggested by Hahn et al. (2007) to the eigenvalues, $\{\lambda_1, \lambda_2, \lambda_3\}$, of the tidal fields smoothed on the linear scale of $R_f = 30 h^{-1} \text{Mpc}$ and then determine the web type of a grid at which each host resides. If all of the tidal eigenvalues, $\lambda_1, \lambda_2, \lambda_3$, at a given grid are positive (negative), then the web-type of the grid is determined to be knot (void). If only the lowest (highest) eigenvalue is negative (positive), then the web-type is filament (sheet). The member clusters belonging to each sample are tagged with the classified web-types of the grids in which their positions lie.

Breaking each of the four q -selected samples into four web type selected subsamples, we redo the whole analysis with the infall-zone satellites around the host clusters belonging to each subsample, the results of which are depicted in Figures 8-9. As can be seen, the same trend of the $\langle \delta v_t \rangle$ - q correlation and $\langle \delta v_r \rangle$ - q anti-correlation is found in the filament and sheet environments. As can be seen, in the highest- q range of $0.9 < q \leq 1$, the values of $\langle \delta v_t \rangle$ exceed those of $\langle \delta v_r \rangle$ for both of the cases of the filaments and sheets. But, note also that while the values of $\langle \delta v_t \rangle$ from the filaments are larger than those from the sheets in the low- q range of $0 < q \leq 0.7$, almost no difference is found in the values of $\langle \delta v_t \rangle$ between the filaments and the sheets in the high- q range of $0.7 < q \leq 1$.

The results shown in Figure 8 contain two crucial implications. First, obstruction of the radial motions of the infall-zone satellites by the weakly coherent tides ($0 < q \leq 0.7$) is the most effective in the filament environments, which is consistent with the claim of Borzyszkowski et al. (2017). Second, obstruction of the radial flow of the satellites by the strongly coherent tides ($0.7 < q \leq 1$) in the sheets can be as effective as in the filaments. For the case of a filament, its thickness was used as an indicator of the tidal coherence (e.g., Borzyszkowski et al. 2017). For the case of a sheet, however, we suggest that the tidal coherence should be best reflected by its *flatness*, predicting that the growths of the hosts embedded in large-scale flat sheets would be delayed by the obstructing effect of the coherent tides on their satellites.

Meanwhile, the knot and void environments yield somewhat different behaviors of $\langle \delta v_t \rangle$ and $\langle \delta v_r \rangle$ against the variation of q (Figure 9). In the range of $0 < q \leq 0.9$, the two mean fractions exhibit the same trends: monotonic increment and decrement of $\langle \delta v_t \rangle$ and $\langle \delta v_r \rangle$ with the increment of q , respectively. However, in the highest- q range of $0.9 < q \leq 1$, abrupt down-turn of $\langle \delta v_t \rangle$ and up-turn of $\langle \delta v_r \rangle$ are witnessed. Note in particular that the void environments yield the lowest value of $\langle \delta v_t \rangle$ in the highest- q range of $0.9 \leq q < 1$ rather than in the lowest- q range, although the errors are large. This result indicates that the coherent tides in the isotropic environments like knots and voids can facilitate the radial motions of the infall-zone satellites rather than obstruct them. It may be explained as follows. In the isotropic environment where \mathbf{e}_1 and \mathbf{e}'_1 are almost perfectly aligned with each other (i.e., $0.9 < q \leq 1$), the direction of \mathbf{e}_3 is also likely to be strongly aligned with \mathbf{e}'_3 . Since in the isotropic knot (void) environments, the gravitational compression (rarefaction) of matter occur along all of the three principal axes simultaneously, the strong \mathbf{e}_3 - \mathbf{e}'_3 alignment will have an effect of facilitating the radial infall of the satellite galaxies onto the host clusters.

Given the results shown in Figures 8-9 that the anisotropic environments like filaments and sheets produce stronger obstructing effect of the tidal coherence, it is suspected that at a given region the tidal coherence q should be correlated with the tidal strength, which is often quantified in terms of the ellipticity, ϵ , of the local potential field as $\epsilon = (\lambda_1 - \lambda_3)/(3 + \delta)$ with $\delta = \sum_{i=1}^3 \lambda_i$ (Yan et al. 2013). To examine whether or not the detected signal of $\langle \delta v_t \rangle$ - q correlation and $\langle \delta v_r \rangle$ - q anti-correlation is at least partly caused by the differences in tidal strengths among the four q -selected samples, we measure the tidal strengths, ϵ , at the locations of the host clusters and determine the ϵ distribution of the host clusters belonging to each sample.

As can be seen in the top panel of Figure 10, the four q -selected samples yield different distributions of $N_h(\epsilon)$, which indicates that the detected signal of $\langle \delta v_t \rangle$ - q correlation and $\langle \delta v_r \rangle$ - q anti-correlation should not be completely independent of the q - ϵ correlation. To nullify the effect of the tidal strengths, we create four resamples of the host clusters according to the values of q , controlling them to have the identical distributions of $N_h(\epsilon)$, which are shown in the bottom panel of Figure 10. Then, we recalculate $\langle \delta v_t \rangle$ and $\langle \delta v_r \rangle$ from the four controlled resamples, which are plotted in Figure 11. As can be seen, the resamples still show clear signals of the $\langle \delta v_t \rangle$ - q correlation and $\langle \delta v_r \rangle$ - q anti-correlation, although the strengths of the signals are slightly reduced compared with the original ones (dotted lines). We emphasize here that since the four controlled resamples have the identical ϵ -distributions, they have no difference in the tidal strengths. If the observed signals of the $\langle \delta v_t \rangle$ - q correlation and $\langle \delta v_r \rangle$ - q anti-correlation from the original samples were completely due to the differences in the tidal strengths among the samples, then the four controlled resamples would yield zero signals. This result confirms the existence of a *dominant* obstructing effect of the tidal coherence q

on the cluster satellites, independent of the q - ϵ correlation.

3. Summary and Discussion

Analyzing the Rockstar halo catalog and density field at $z = 0$ from the SMDPL (Klypin et al. 2016), we have located the infall-zone satellites ($M_s \geq 10^{11} h^{-1} M_\odot$) around the host clusters ($M_h \geq 10^{14} h^{-1} M_\odot$) in the distance range of $1 \leq r/r_v < 3$, and then determined two directions of the major principal axes of the tidal field smoothed on the scales of $2 h^{-1} \text{Mpc}$ and $30 h^{-1} \text{Mpc}$ at the position of each host. Calculating the tidal coherence, q , as the alignments between the two directions of the major principal axes for each cluster, we have created four q -selected samples of the host clusters in the ranges of $0 < q \leq 0.4$, $0.4 < q \leq 0.7$, $0.7 < q \leq 0.9$ and $0.9 < q \leq 1$. For each sample, we have measured the tangential and radial components of the relative velocities of the infall-zone satellites around the hosts and taken the mean values (Figure 1). It has turned out that a sample with a higher q value yields significantly higher and lower mean fractions of the tangential and radial velocities of the infall-zone satellites, respectively (Figure 2).

Creating the four q -selected resamples of the host clusters which are controlled to have identical distributions of M_h and r (Figures 3-4), we have computed the mean values of the tangential and radial velocities from each of the controlled samples. It has been found that the mean radial velocity decreases monotonically with q in the entire range of q while the mean tangential velocity shows slight increase with q in the range of $0 < q \leq 0.7$ and a rapid rise in the range of $0.9 < q \leq 1$. Our interpretation of the results shown in Figures 2-5 is that the gravitational compression of matter along the major principal axis whose direction is coherent over widely separated scales (i.e., the coherent tide) has an effect of significantly obstructing the radial motions of the infall-zone satellites toward the host clusters, while it tends to facilitate their tangential motions.

We have also investigated if and how the obstructing effect of the coherent tides depends on the satellite mass, separation distance and web-type of the large-scale environment. It has been shown that the infall-zone satellites having lower masses ($M_s \leq 5 \times 10^{11} h^{-1} M_\odot$), located in the inner infall zone ($1 \leq r/r_v < 2$), and surrounded by the anisotropic environments like filaments and sheets are more vulnerable to the obstructing effect of the coherent tides than the other cases (Figures 6-8). No matter what distances and masses the infall-zone satellites have, their mean fractions of the tangential velocities have been found to monotonically increase with the increment of q . However, in the isotropic large-scale environments like knots and voids, the mean fractions of the tangential velocities exhibit abrupt decrease rather than increase in the highest- q range, $0.9 < q \leq 1$ (Figure 9). To explain this phenomenon,

we have noted that the almost perfect alignments of the major principal axes of the tidal fields between the linear and nonlinear scales (i.e., $0.9 < q \leq 1$) would induce the strong alignments of the minor principal axes. Since in the isotropic environments the gravitational compression of matter occur concurrently along all of the three principal axes of the tidal fields, the radial infall of the satellite galaxies onto the host clusters will be facilitated rather than obstructed by the gravitational compression of surrounding matter distribution along the coherent directions of the minor principal axes in the isotropic environments with highest tidal coherence.

In this work, we have implicitly assumed that the web-classification algorithm of Hahn et al. (2007) can be used to determine the web types of environments even when the tidal fields are smoothed on the linear scale of $R_f = 30 h^{-1}\text{Mpc}$. However, it has to be mentioned here that this assumption has yet to be justified since the previous works which tested this algorithm usually considered much smaller scales, $R_f \leq 5 h^{-1}\text{Mpc}$ (e.g., see Hahn et al. 2007; Libeskind et al. 2018). It will be necessary to examine up to what scale this algorithm is applicable for the determination of the web types, which is, however, beyond the scope of this Letter.

We have also nullified the dependence of the obstructing effect of the tidal coherence on the tidal strengths by creating the four q -selected resamples of the host clusters which have identical distributions of the ellipticities of the potential field (a measure of the tidal strength). Showing that the four resamples still yield clear signals of the correlations (anti-correlations) between the mean fractions of the tangential (radial) velocities and the degree of the tidal coherence, we have confirmed that the obstructing effect of the tidal coherence on the cluster satellites is independent of and dominant over the effect of the tidal strengths (Figures 10-11).

Although our observational evidence for the obstructing effect of the coherent tides has been found from the cluster satellites rather than from the galaxy ones, we believe that it can be used to explain the recently discovered anti-correlation between the tidal coherence and the galaxy luminosity from the SDSS DR10 (Lee 2018a): The galaxies located in the regions with higher tidal coherence are less luminous, because the coherent tides facilitate the tangential motions of the satellites and obstruct their radial flow onto the host galaxies, as conjectured by Lee (2018a). Our study also provides a fundamental explanation for the phenomenon found by Pandey & Bharadwaj (2006) that the spatial distributions of the less luminous galaxies tend to be more anisotropic. The highly coherent tides often produce large-scale bulky filaments and flat sheets in which the spatial distributions of the galaxies are highly anisotropic. Thus, the observed link of the luminosities of the galaxies with the anisotropic shape of the large-scale structure where they reside is in fact a reflection of the

strong obstructing effect of the coherent tides.

As mentioned in Section 1, this work was motivated and inspired by the recent numerical study of Borzyszkowski et al. (2017) which revealed that the growth history of the galaxies depend on the thickness of the host filaments. Our findings supports their idea, and extends its validity to the cluster scales and to the other types of the cosmic web by showing that the obstruction of the radial motions of the cluster satellites by the coherent tides occur not only in the filaments but also in the sheets, knots and voids. Given the current results obtained from the cluster satellites at $z = 0$, we expect that the lower-mass galaxy satellites must be much more vulnerable to the obstructing effect of the coherent tides than the cluster satellites. We also expect that the coherent tides must have a weaker obstructing effect at higher redshifts since the gravitational compression of matter along the major principal axes of the large-scale tidal fields at higher redshifts would be incomplete. In the isotropic environments like knots and voids, however, the effect of the tidal coherence is expected to be stronger at higher redshifts than at $z = 0$. Our future work is in the direction of testing these expectations against numerical data from N-body simulations with much higher resolution.

The CosmoSim database used in this paper is a service by the Leibniz-Institute for Astrophysics Potsdam (AIP). The MultiDark database was developed in cooperation with the Spanish MultiDark Consolider Project CSD2009-00064. I gratefully acknowledge the Gauss Centre for Supercomputing e.V. (www.gauss-centre.eu) and the Partnership for Advanced Supercomputing in Europe (PRACE, www.prace-ri.eu) for funding the MultiDark simulation project by providing computing time on the GCS Supercomputer SuperMUC at Leibniz Supercomputing Centre (LRZ, www.lrz.de). The Bolshoi simulations have been performed within the Bolshoi project of the University of California High-Performance AstroComputing Center (UC-HiPACC) and were run at the NASA Ames Research Center.

I am grateful to an anonymous referee for very helpful comments which helped me correctly interpret the final result of the current work. I acknowledge the support of the Basic Science Research Program through the National Research Foundation (NRF) of Korea funded by the Ministry of Education (NO. 2016R1D1A1A09918491). I was also partially supported by a research grant from the NRF of Korea to the Center for Galaxy Evolution Research (No.2017R1A5A1070354).

REFERENCES

- Ahn, C. P., Alexandroff, R., Allende Prieto, C., et al. 2014, *ApJS*, 211, 17
- Behroozi, P. S., Wechsler, R. H., & Wu, H.-Y. 2013, *ApJ*, 762, 109
- Borzyszkowski, M., Porciani, C., Romano-Díaz, E., & Garaldi, E. 2017, *MNRAS*, 469, 594
- Gao, L., & White, S. D. M. 2007, *MNRAS*, 377, L5
- Garaldi, E., Romano-Díaz, E., Borzyszkowski, M., & Porciani, C. 2017, *arXiv:1707.01108*
- Hahn, O., Porciani, C., Carollo, C. M., & Dekel, A. 2007, *MNRAS*, 375, 489
- Klypin, A., Yepes, G., Gottlöber, S., Prada, F., & Heß, S. 2016, *MNRAS*, 457, 4340
- Lee, J. 2018a, *ApJ*, 867, 36
- Lee, J. 2018b, *arXiv:1808.08559*
- Libeskind, N. I., van de Weygaert, R., Cautun, M., et al. 2018, *MNRAS*, 473, 1195
- Pandey, B., & Bharadwaj, S. 2006, *MNRAS*, 372, 827
- Pandey, B., & Sarkar, S. 2017, *MNRAS*, 467, L6
- Press, W. H., Teukolsky, S. A., Vetterling, W. T., & Flannery, B. P. 1992, Cambridge: University Press, —c1992, 2nd ed.,
- Planck Collaboration, Ade, P. A. R., Aghanim, N., et al. 2014, *A&A*, 571, A16
- Riebe, K., Partl, A. M., Enke, H., et al. 2013, *Astronomische Nachrichten*, 334, 691
- Yan, H., Fan, Z., & White, S. D. M. 2013, *MNRAS*, 430, 3432
- Zu, Y., Weinberg, D. H., Jennings, E., Li, B., & Wyman, M. 2014, *MNRAS*, 445, 1885

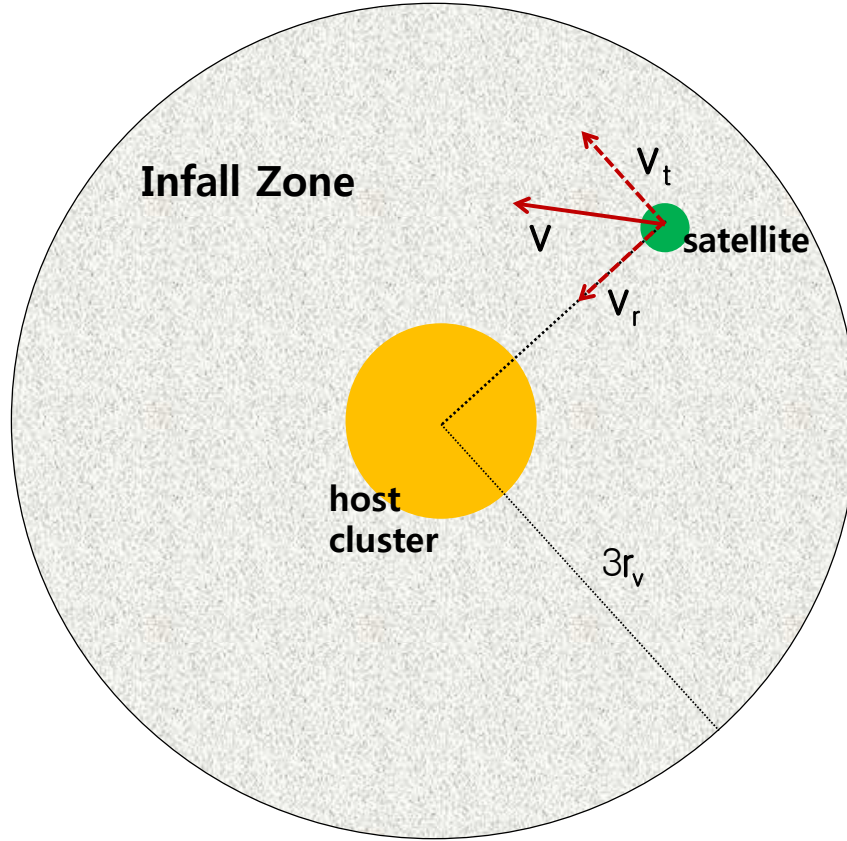


Fig. 1.— Illustration of an infall-zone satellite whose comoving peculiar velocity \mathbf{v} can be decomposed into a radial (\mathbf{v}_r) and a tangential (\mathbf{v}_t) component in the infall zone around a host cluster with virial radius r_v .

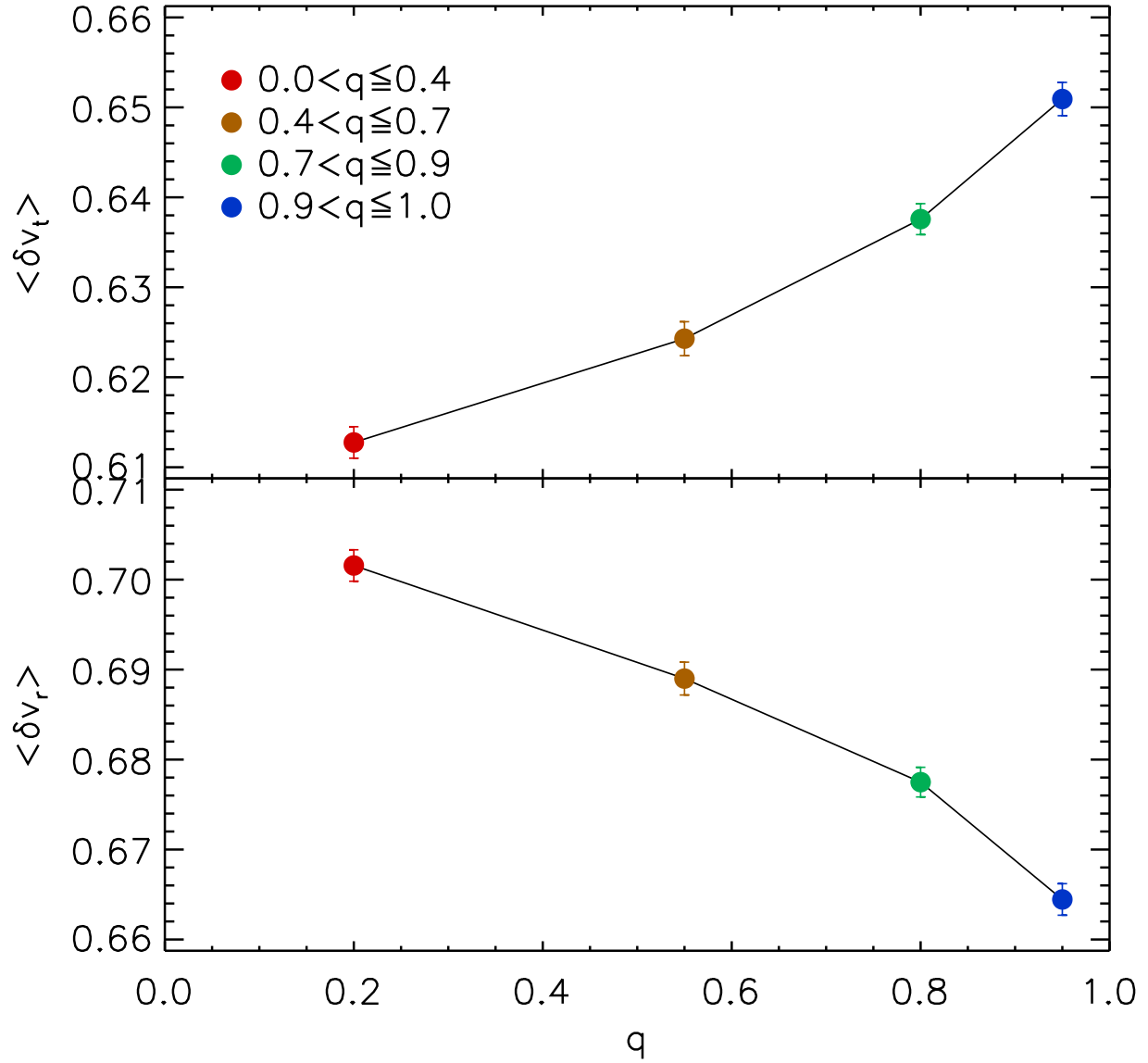


Fig. 2.— Mean fractions of the tangential and radial velocities of the infall-zone satellites versus the tidal coherence, q , in the top and bottom panels, respectively.

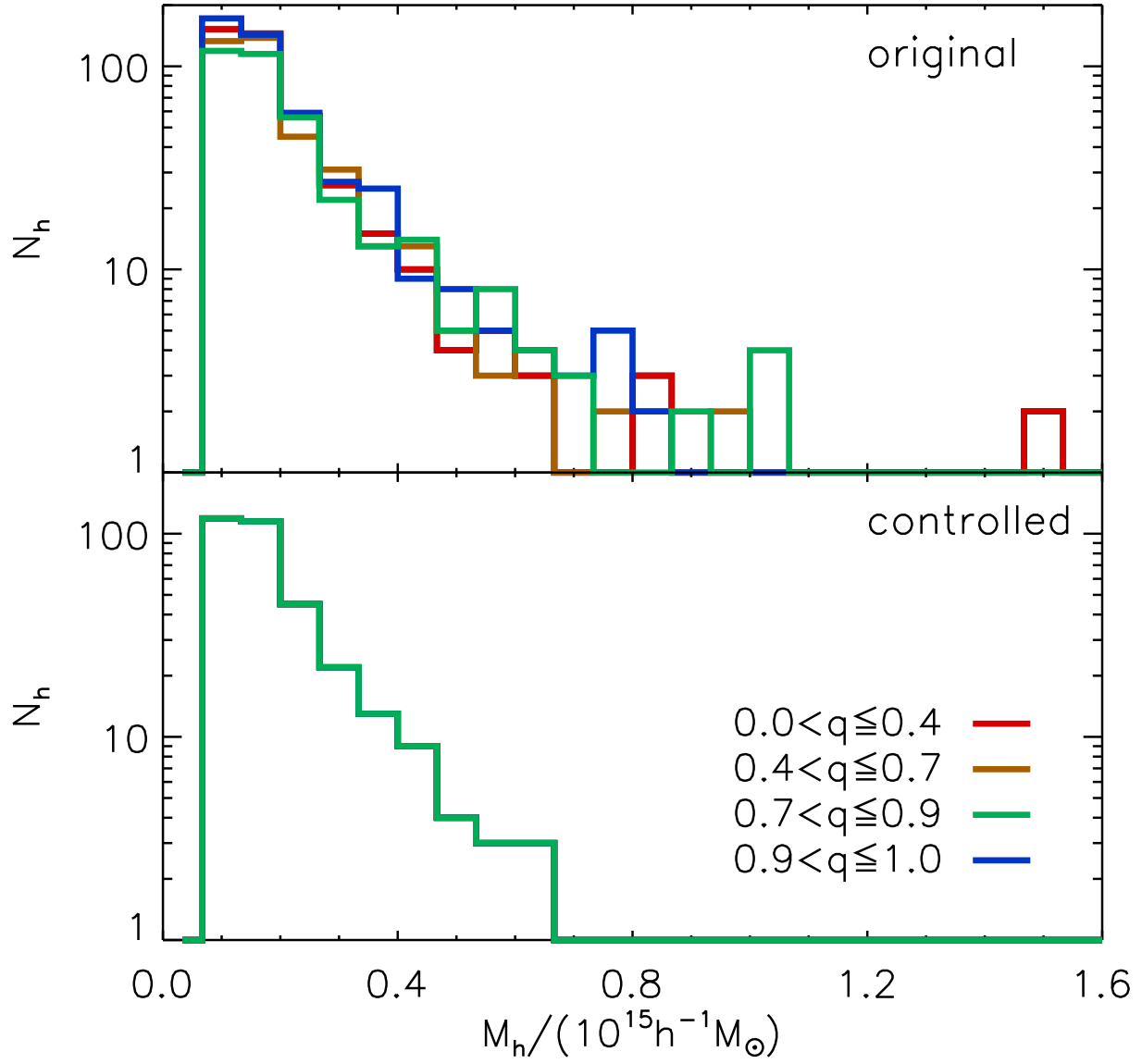


Fig. 3.— Original (top panel) and controlled (bottom panel) number distributions of the clusters as a function of their virial masses from four q -selected samples.

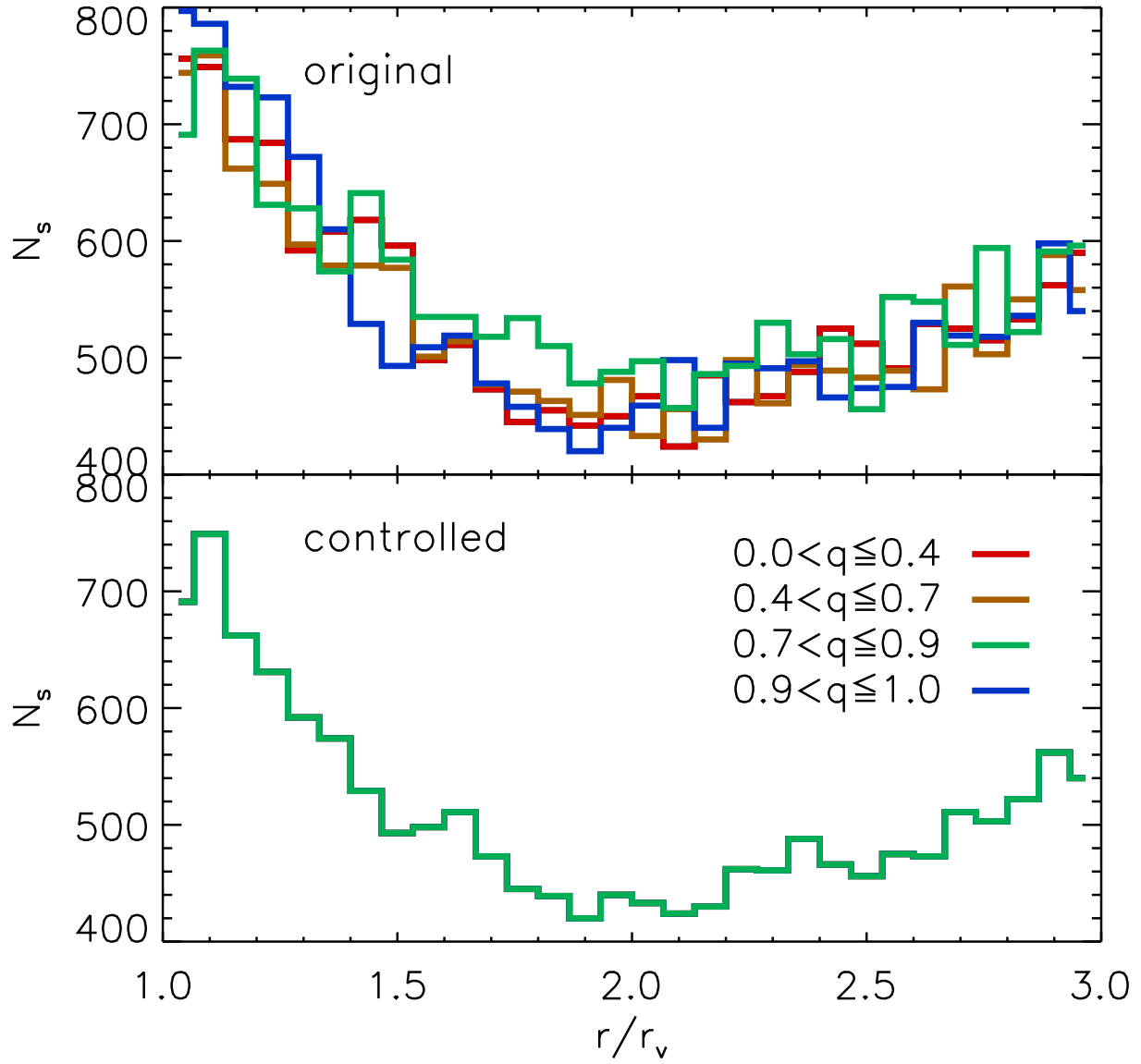


Fig. 4.— Original (top panel) and controlled (bottom panel) number distributions of the infall-zone satellites as a function of their separation distances from the centers of their hosts from the four q -selected samples.

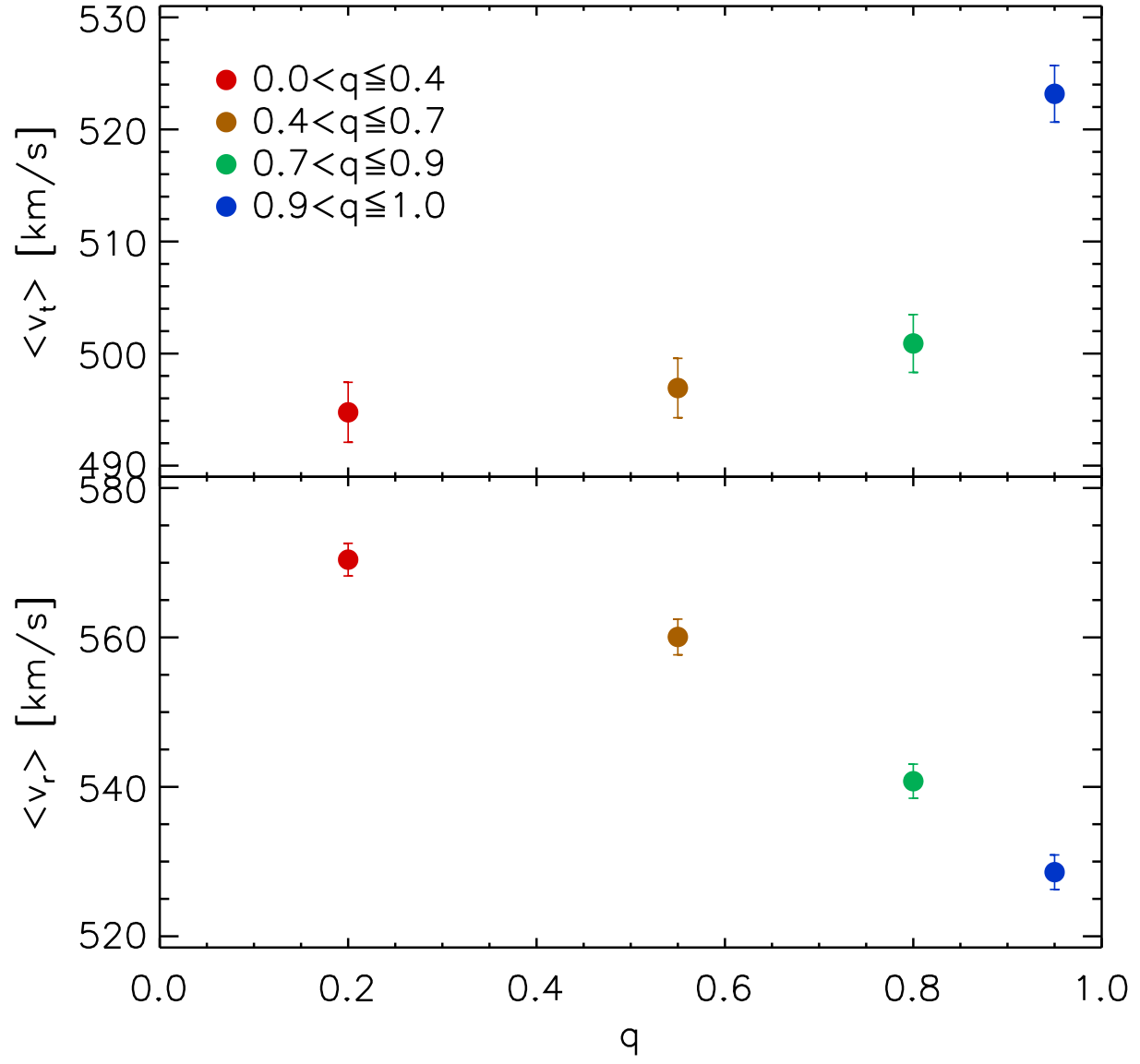


Fig. 5.— Mean tangential and radial velocities of the infall-zone satellites from the controlled resamples versus q in the top and bottom panels, respectively.

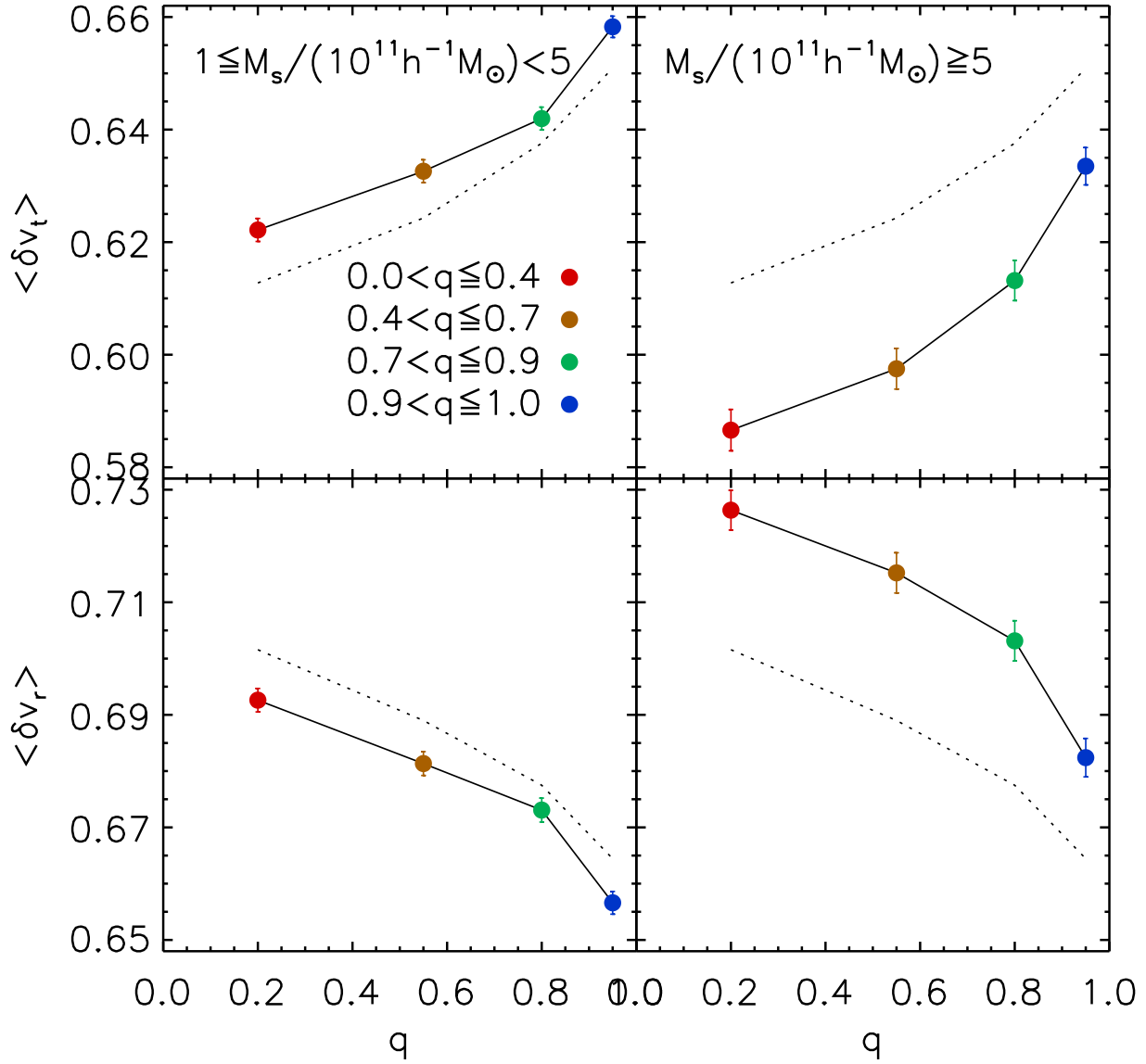


Fig. 6.— Same as Figure 2 but averaged over the low-mass (left panel) and high-mass (right panel) infall-zone satellites separately. The results shown in the top and bottom panels of Figure 2 are also shown as dotted lines here for comparison.

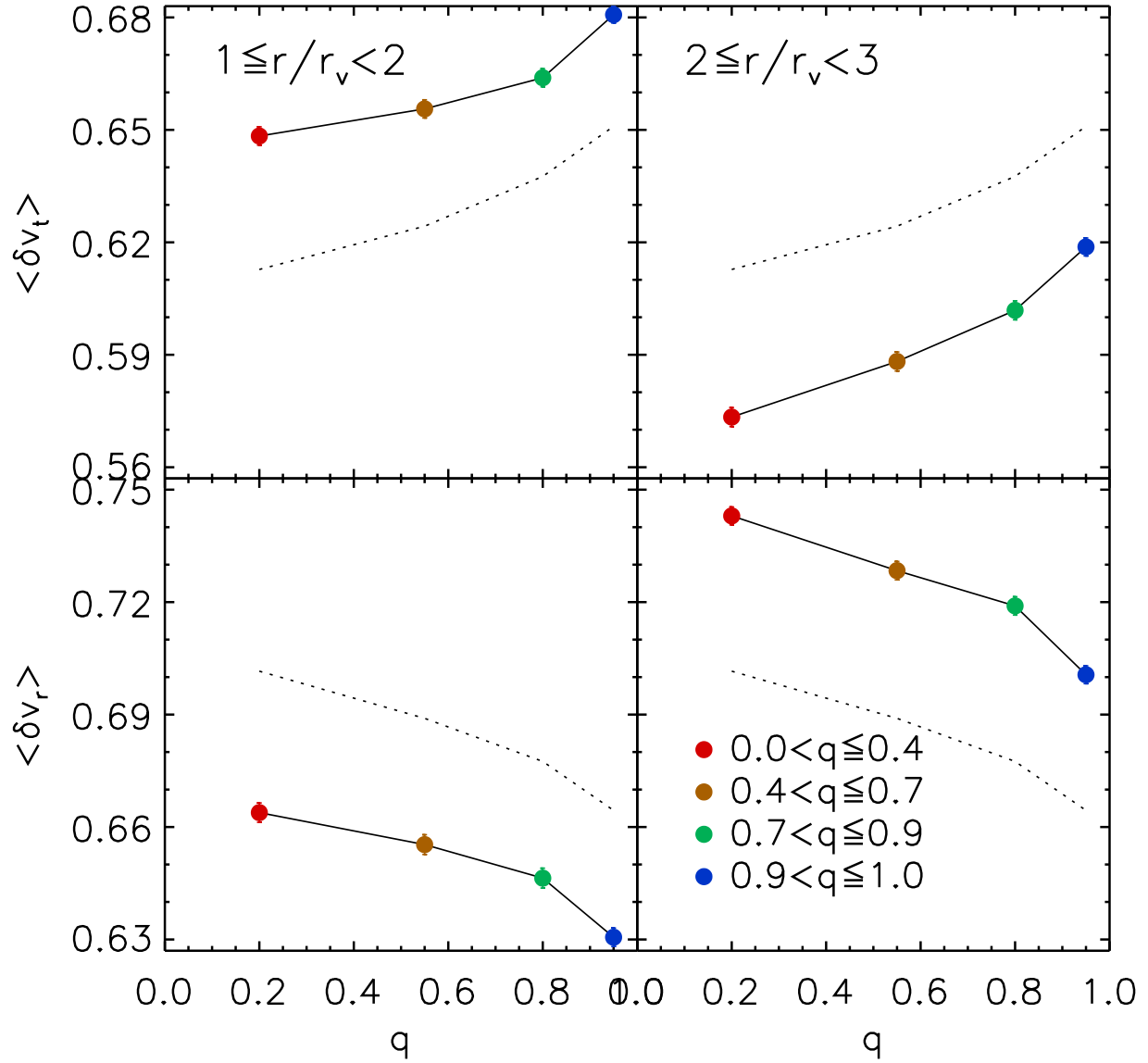


Fig. 7.— Same as Figure 2 but averaged over the inner (left panel) and outer (right panel) infall-zone satellites separately.

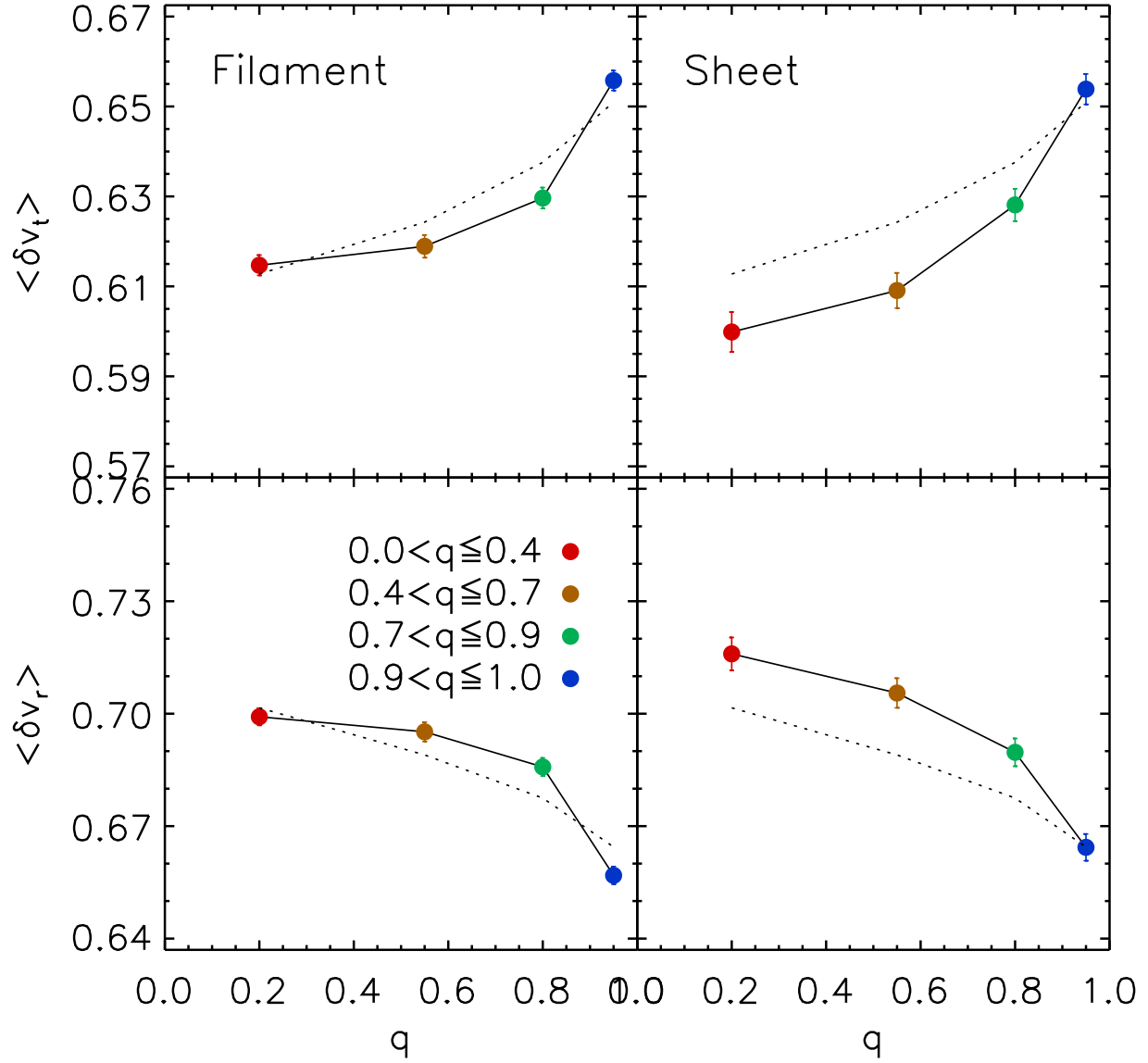


Fig. 8.— Same as Figure 2 but averaged over the infall-zone satellites around the clusters embedded in the filaments (left panel) and sheets (right panel) separately.

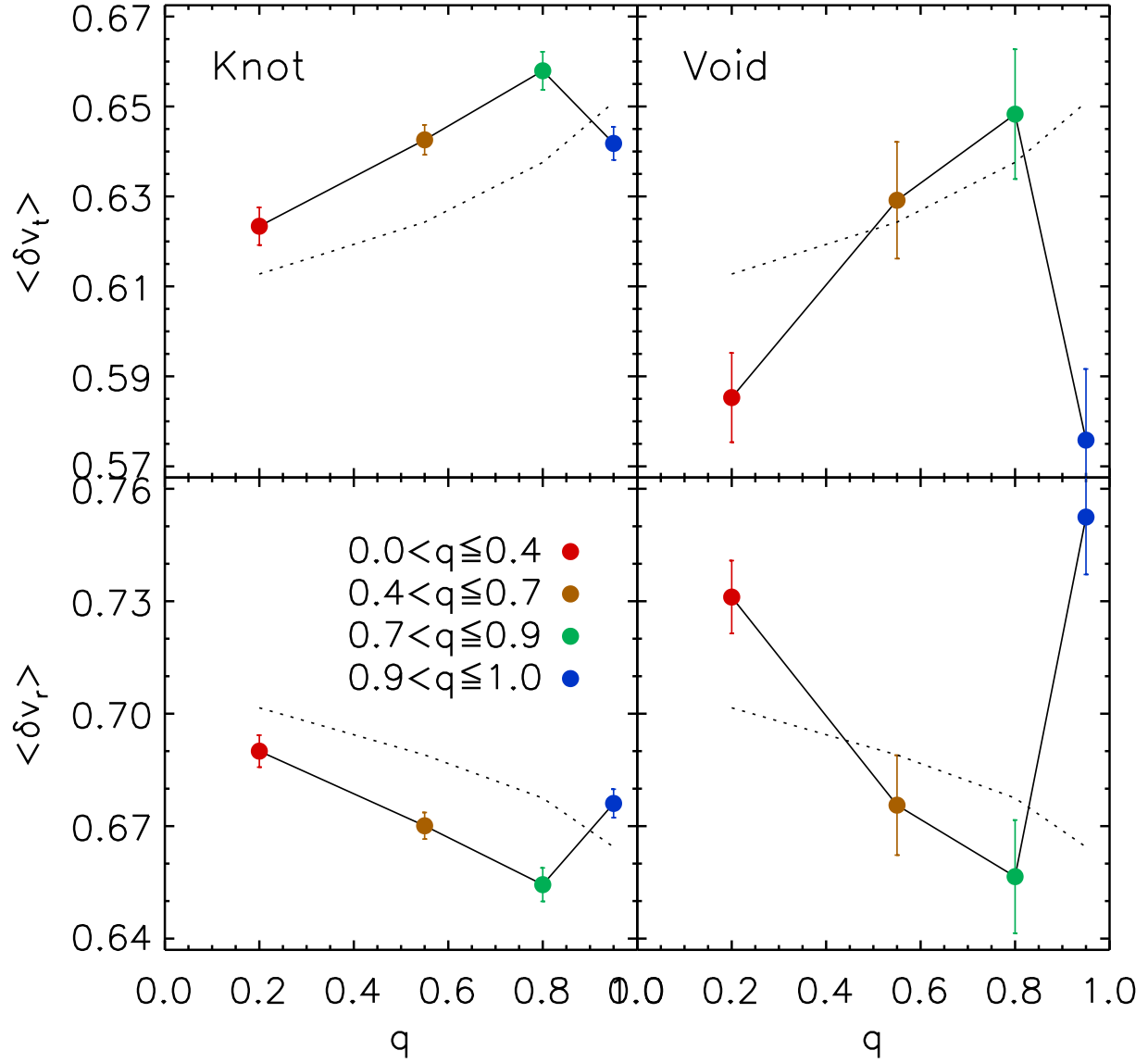


Fig. 9.— Same as Figure 2 but averaged over the infall-zone satellites around the clusters embedded in the knots (left panel) and voids (right panel) separately.

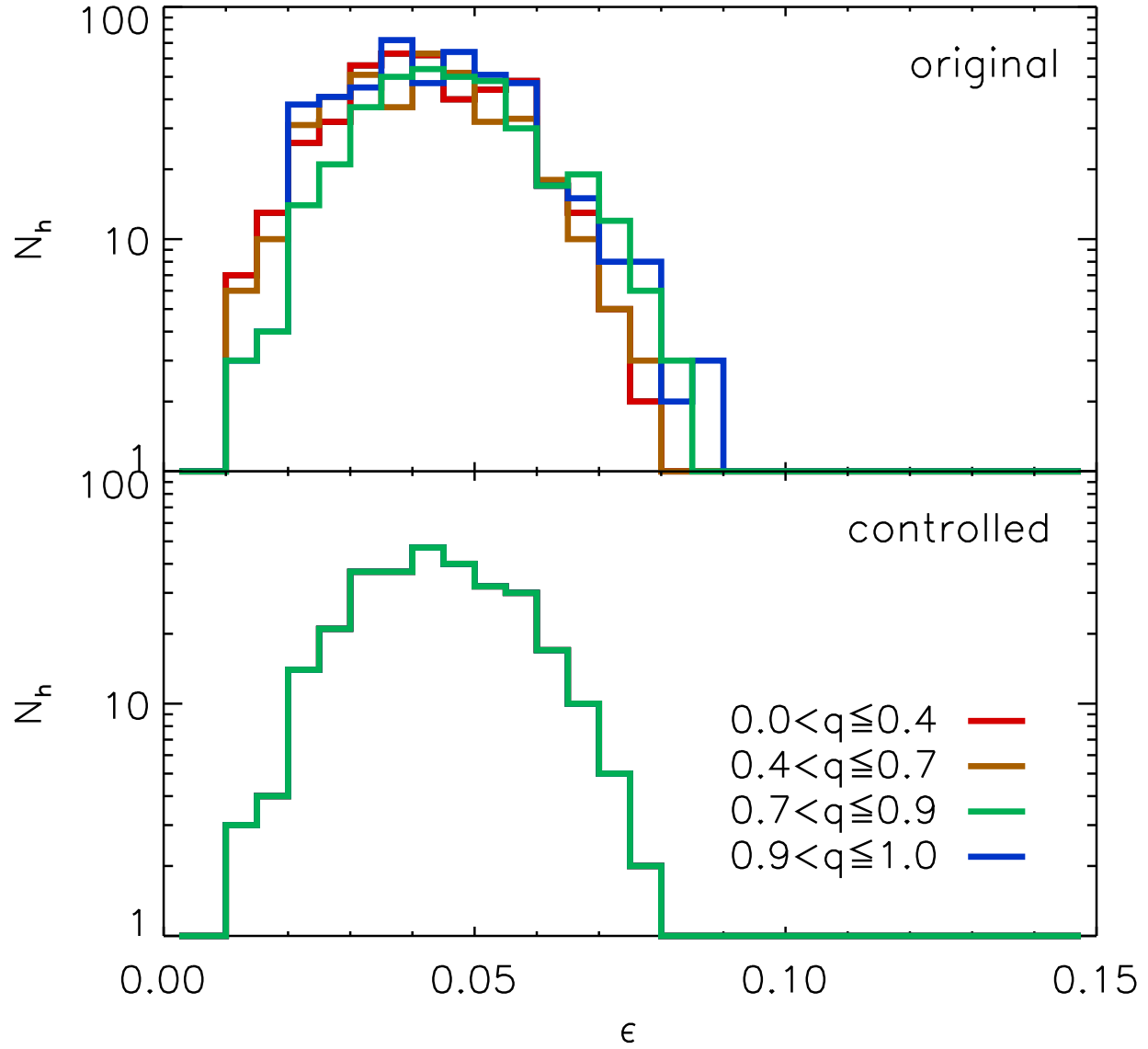


Fig. 10.— Original (top panel) and controlled (bottom panel) number distributions of the clusters as a function of the ellipticities of the regions where the host clusters are located.

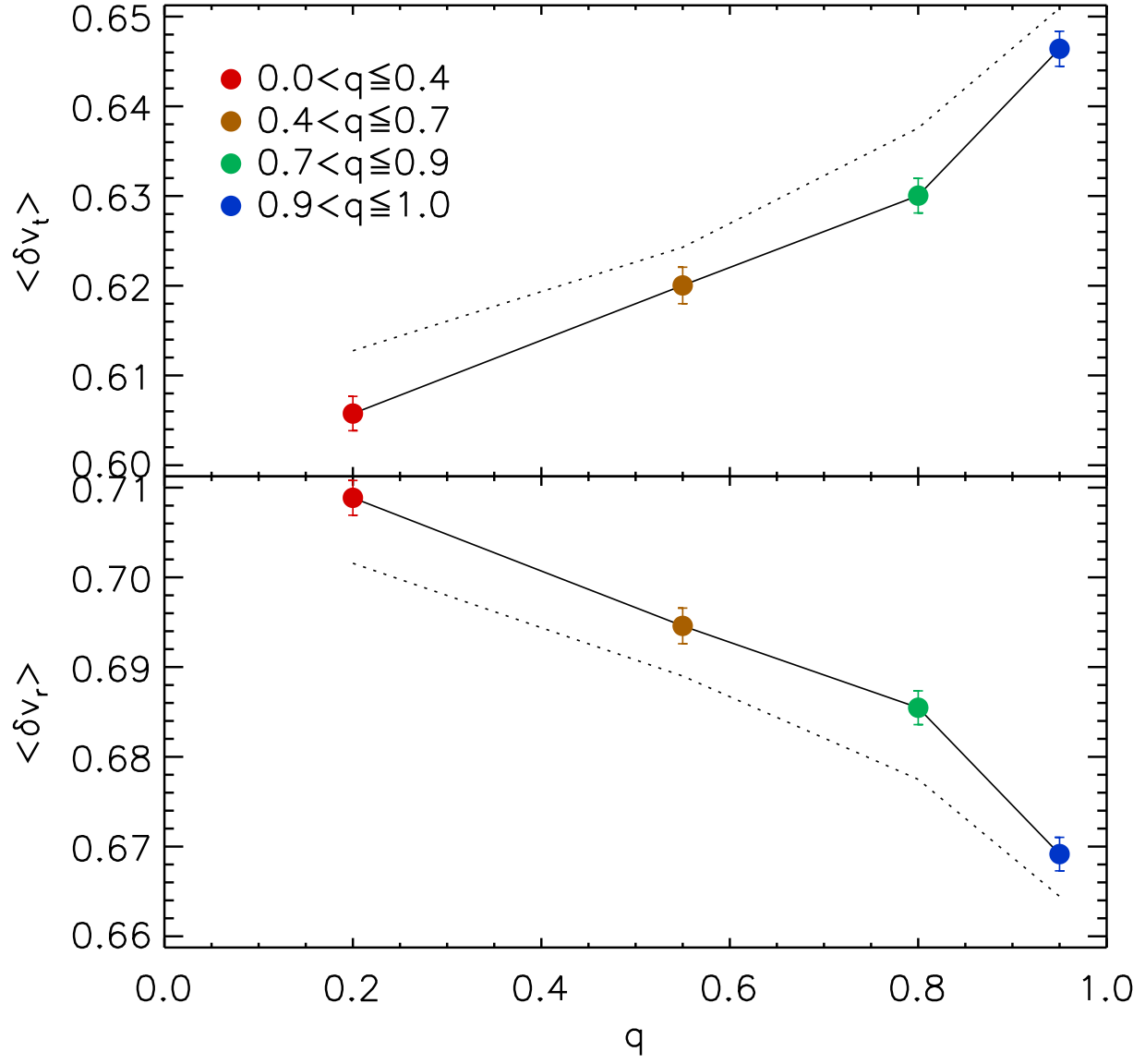


Fig. 11.— Same as Figure 2 but from the controlled resamples of the host clusters.

Table 1. Cluster numbers and mass ranges from four q -selected samples

q	N_h	M_h ($10^{14} h^{-1} M_\odot$)
(0.0, 0.4]	429	[1.0, 17.1]
(0.4, 0.7]	395	[1.0, 12.8]
(0.7, 0.9]	466	[1.0, 14.9]
(0.9, 1.0]	369	[1.0, 14.4]